Quantitative tests revealing hydrogen enhanced dislocation motion in α-iron

Long-Chao Huang
Xi'an Jiaotong University https://orcid.org/0000-0001-7832-7271
Dengke Chen
Shanghai Jiao Tong University https://orcid.org/0000-0001-7986-0019
De-Gang Xie
Xi'an Jiaotong University
Suzhi Li
Xi'an Jiaotong University https://orcid.org/0000-0003-1113-6555
Ting Zhu
Georgia Institute of Technology https://orcid.org/0000-0001-8612-9689
Dierk Raabe
Max-Planck-Institut für Eisenforschung https://orcid.org/0000-0003-0194-6124
Evan Ma
Johns Hopkins University
Ju Li
Massachusetts Institute of Technology https://orcid.org/0000-0002-7841-8058
Zhi-Wei Shan (zwshan@mail.xjtu.edu.cn)
Xi'an Jiaotong University https://orcid.org/0000-0002-4533-0869

Article

Keywords:

Posted Date: November 23rd, 2021

DOI: https://doi.org/10.21203/rs.3.rs-1059604/v1

Version of Record: A version of this preprint was published at Nature Materials on April 20th, 2023. See the published version at https://doi.org/10.1038/s41563-023-01537-w.

Abstract

Hydrogen embrittlement jeopardizes the use of high-strength steels as critical load-bearing components in energy, transportation, and infrastructure applications. However, our understanding of hydrogen embrittlement mechanism is still obstructed by the uncertain knowledge of how hydrogen affects dislocation motion, due to the lack of quantitative experimental evidence. Here, by studying the well-controlled, cyclic, bow-out movements of individual screw dislocations, the key to plastic deformation in α-iron, we find that the critical stress for initiating dislocation motion in a 2 Pa electron-beam-excited H_2 atmosphere is 27~43% lower than that under vacuum conditions, proving that hydrogen lubricates screw dislocation motion. Moreover, we find that aside from vacuum degassing, dislocation motion facilitates the de-trapping of hydrogen, allowing the dislocation to regain its hydrogen-free behavior. Atomistic simulations reveal that the observed hydrogen-enhanced dislocation motion arises from the hydrogen-reduced kink nucleation barrier. These findings at individual dislocation level can help hydrogen embrittlement modelling in steels.

Main Text

Steels, consisting mainly of iron, constitute the most important workhorse material class of our modern society, often serving in parts of vital importance, be it in power plants, vehicles, buildings or critical infrastructures. In the coming of a hydrogen-based economy, however, this critical function is at risk due to hydrogen embrittlement, a sudden and often catastrophic deterioration of the material's load-bearing capacity. While multiple hydrogen embrittlement (HE) models, such as hydrogen-enhanced localized plasticity (HELP)[1,2], hydrogen-enhanced decohesion[3] and hydrogen-stabilized superabundant strain-induced vacancies[4] have been proposed, consensus has yet to be reached on the effects of these mechanisms. Also, direct experimental proof of the influence of hydrogen at the single defect scale is missing. The latter problem can be attributed to the fact that hydrogen is the smallest and fastest among all solute atoms, which makes it difficult to probe into its influence on individual lattice defects. Also, challenges arise from the formidable complexity of the HE phenomenon, owing to the often-intricate interplay of several mechanisms. Consequently, some of the reported macroscopic observations are contradictory and, in many cases, it is difficult to associate hydrogen-related macroscopic embrittlement with one distinct lattice defect type and mechanism. At the macroscale, hydrogen has been shown to cause both hardening and softening in pure iron[5,6], while in regions below the fracture surface, hydrogen has been found to be able to either enhance[7,8] or reduce plastic activity[9,10]. At the micro- and nanoscales, and even at atomic scales, the main debate revolves around the question of the effect of hydrogen on the kinetics of dislocations[11–16]. According to the classic Cottrell and Snoek theories, diffusible interstitial atoms including hydrogen are expected to form an atmosphere around the dislocation, causing a drag to dislocation motion[17,18]. Interestingly, Birnbaum, Robertson and coworkers observed the opposite, namely, the mobility of dislocations was enhanced in several metallic materials, including α-titanium[19], aluminum[20], nickel[21], 316 austenitic steel[22] and α-iron[23]. They attributed this effect to elastic shielding of the dislocation's stress field by the hydrogen atmosphere that was assumed to surround the dislocation core. The H-enhanced dislocation mobility was proposed as the “root cause” of HE, serving as core evidence for the HELP theory[2]. However, these results have been challenged by recent atomistic simulations, which did not reproduce H-enhanced dislocation mobility but instead demonstrated a hydrogen-induced drag effect in aluminum[24] and α-iron[25]. On the experimental side, we confirmed some of these theoretical hypotheses, viz. a hydrogen-induced pinning effect of dislocations[24], only for the case of aluminum, which has a face-centered-cubic (FCC) structure and contains dislocations with narrow planar cores of dissociated leading and trailing partials. For metals with a body-centered-cubic (BCC) structure, such as α-iron, tungsten etc., the motion of screw dislocation via kink pair formation and propagation is the rate controlling process of the deformation at room temperature, owing to the non-planar, three-fold symmetry of the screw dislocation core[26,27]. However, direct experimental observations that clearly reveal the hydrogen effect on kink pair formation and the associated screw dislocation motion at a single defect scale is still lacking, although hints from theory exist[14,15,28–30].

The classic works by Birnbaum, Robertson and coworkers were based on the use of environmental transmission electron microscopy (ETEM), introducing H_2 at several thousand pascals, in conjunction with special straining holders to impose constant stress or constant strain boundary conditions to metal foil specimens[23,31]. Their experimental setup was designed to change the hydrogen atmosphere during or after dislocation glide[19–23]. However, to reach unequivocal interpretation of their observations, there are a few unclear issues that motivated us to develop an alternative experimental setup for revisiting the hydrogen effect on dislocation mobility. Firstly, before introducing hydrogen into the ETEM chamber, the observed dislocations were usually at rest[20–22], thus making it impossible to observe any hydrogen-related drag or pinning effects. Secondly, when thousands of pascals of H_2 were flooded into or pumped out of the ETEM chamber within a few seconds, this might have altered either the local distribution of the internal stress or the external load which had been assumed to remain constant. These effects might have affected the initially resting dislocations, triggering their motion due to their high sensitivity to stress. Finally, it is generally difficult to preclude surface notch and bending effects and the associated stresses on dislocation motion in such thin foil experiments. Also, as the dislocations observed usually have their ends pinned on the foil surfaces[19,22,23], the velocity of dislocation motion would be largely determined by the destabilization rate of pinning points and the spacing between them. However, dislocation pinning can be altered by hydrogen adsorption on metal surfaces under electron beam illumination, especially in the case of hydrogen-induced reduction of the surface oxides (which are otherwise always present) or removal of organic contaminants from the surface[32]. These considerations fuel our motivation to perform well-controlled experiments that are capable of reducing substantially the impact of these factors, particularly related to uncontrolled surface pinning of dislocations, ill-defined surface reaction effects that may cause changes in the mechanical boundary conditions, as well as variable stress effects due to the use of thin foils. Avoiding these experimental constraints is essential for conducting well-controlled experiments, thereby gaining unequivocal experimental evidence for the effect of hydrogen on individual dislocations.

In this work, we designed a new and fully quantitative in situ ETEM mechanical testing protocol, as illustrated in Fig. 1, which enables the observation and comparison of the bow-out motion of the same dislocation segments under both vacuum and hydrogen-containing atmospheric conditions. To avoid the thin-foil problems above, we prepared submicron-sized free-standing cylindrical α-iron pillars, which were subjected to cyclic stresses with the aim to remove most of the pre-existing dislocations (referred to as the mechanical annealing effect[33]) while retaining a few individually isolated dislocations that exhibited stable bow-out configuration and well-controlled motion between the pinning points (Fig. 1b and c). The controlled dislocation motion was exactly repeated in series of multiple consecutive testing cycles by maintaining a constant cyclic stress of low magnitude (locally depending on bow-out stress), thus allowing for quantifying the variation in the dislocation's response upon varied environments in a highly controlled manner, as shown in Fig. 1d. The uniaxial compressive loading mode combined with in situ observation allows us to quantify the stress required for activating the movement of each individual dislocation and its glide distance, alternatingly in vacuum and under hydrogen atmosphere, respectively.

A pillar with top diameter of ~300 nm was prepared for the cyclic compression tests. As shown in Fig. 2a, a platinum layer of ~150 nm in thickness was applied on the pillar top to protect it from non-uniform contact with the diamond punch during the multiple compression tests, thereby avoiding additional contact-induced dislocation emission. This design detail provided well-defined, controlled and repeatable contact boundary conditions. The as-fabricated single-crystal iron pillar contained a high dislocation density, making it difficult to track the behavior of individual dislocations, without the optical and mechanical influence of neighboring dislocations. To reduce the dislocation density inside the pillar to a small value, allowing for their individual observation, we applied the mechanical annealing treatment, which contains a set of moderate cyclic compression and relaxation loading operations to promote dislocation escape and annihilation (see Supplementary Fig. 1). Since the Peierls stress of screw dislocations is at least one order of magnitude larger than that of edge dislocations in BCC crystals at zero temperature due to their non-planar core[34], the mobility of screw components of a general curved dislocation is intrinsically much lower than that of edge components. It follows that the applied stress will drive the edge components out of the pillar first, so that after this mechanical treatment, most mixed dislocations had been transformed into pure screw ones with a Burgers vector ½<111>, as shown by the characterization results presented in Supplementary Fig. 2 and Supplementary Table 1. Such screw dislocations usually form long straight lines along the <111> Peierls valleys, pinned by dislocation jogs or at surfaces, as shown in Fig. 1b. Under an applied shear stress, movement of these dislocations usually starts from the longest free dislocation segments between pinning points, gradually changing its shape from a straight into a bowed-out dislocation, as shown in Fig. 1c, a process thus referred to as bow-out motion hereafter. Upon unloading, the dislocation segment springs back to its original equilibrium shape/position, indicating that the bow-out motion is reversible and no new pinning in the temporarily sheared region had taken place. Therefore, by gradually lowering the peak stress in the ensuing mechanical cycles we maintained these stable and reversible bow-out configurations, neither adding nor removing pinning points. In this way we were able to reproduce the motion of the exact same dislocation segment in a well-defined and fixed local position hundreds of times, enabling the quantitative and repeatable observation and comparison of its kinetic parameters across different loading atmospheres (Fig. 1d). Compared with previous experiments, this experimental setup minimizes the influence on dislocation motion arising from the variation of surface and boundary conditions and inhomogeneous stress landscapes.

Figure 2a shows a typical dislocation (marked as #1) that exhibited stable and fully reversible bow-out motion under cyclic compression, thus suitable for detailed observation and analysis under the two different types of atmospheric conditions (vacuum versus hydrogen). The dislocation was identified as a dominantly screw-type defect with its Burgers vector ½<111> and slip plane {112} (see Supplementary Fig. 2 and 3), constituting the slip system {112}<111>. The atmospheric control experiments started with a testing session under vacuum (before hydrogenation), which consisted of a total of 11 consecutive load cycles numbered N = 1-11 (Supplementary Movie 1). Identical load-time functions were applied to all cycles, corresponding to a normal stress oscillation between the valley stress (σ_{min}) of ~21 MPa and the peak stress (σ_{max}) of ~211 MPa. After confirming that the bow-out motion was stable, fully reversible and reproducible in this first vacuum test run, we exposed the sample to a ~2 Pa H_2 under electron illumination for about 2 hours. Previous experiments have shown that when the 2 Pa H_2 is excited by the high voltage electron beam, the equivalent fugacity can reach hundreds of MPa[35,36]. Using Sieverts' law[28] and 500 MPa hydrogen fugacity, the equilibrium bulk hydrogen concentration in iron was estimated to be ~2 atomic ppm. Although the local hydrogen concentration at the dislocation core may be much higher than this value, the dislocation configuration was confirmed to remain unchanged throughout the hydrogenation process, as shown in Supplementary Fig. 4.

We then applied the same load-time function for the ensuing load cycles (renumbered N = 1, 2…), after hydrogenation (see Supplementary Movie 2). The movement of dislocation #1 was compared before and after hydrogen exposure. After hydrogenation, we can see that under the same cyclic stress, the bow-out movement of dislocation #1 displayed an enlarged amplitude, as indicated by the comparison between its configuration at σ_{max} in vacuum and in hydrogenated state (Fig. 2b). To further quantify the hydrogenation-induced change in dislocation motion, we performed a frame-by-frame correlation between loading time/stress and the position of dislocation #1 in the movie recorded during the whole in situ tests. In each cycle, the movement of dislocation #1 was activated only when the applied stress increased above a critical value, which we referred to as dislocation activation stress (σ_{c}). Then the dislocation continued to move, until reaching the maximum projected glide displacement (δ_{max}) at the peak stress σ_{max}, as shown in Fig. 2c. The measurement results of δ_{max} and σ_{c} in each cycle, as shown in Fig. 2d and 2e, confirmed that the glide of dislocation #1 after hydrogenation can reach a larger distance than that under vacuum, and the average δ_{max} increased by ~65% from 10.8±0.6 nm in vacuum to 17.8±3.3 nm under hydrogen. Moreover, the average value for σ_{c} was reduced by ~28% from 104.8±7.4 MPa to 5.6±8.0 MPa after hydrogenation. Using the Schmid factor of 0.471 for the {112}<111> slip system, the critical resolved shear stress (τ_{c}) for the activation of dislocation #1 can be calculated as 49.4±3.5 MPa and 35.6±3.8 MPa before and after hydrogenation, respectively. These effects of hydrogen on the motion of the screw dislocation were further corroborated by another group of controlled experiments (Supplementary Note 1; Supplementary Fig. 5; Supplementary Movie 3 and Movie 4), with the dislocation motion showing ~27% lower σ_c and ~64% larger δ_{max} after hydrogenation. Therefore, our experimental results prove that the screw dislocation moves easier (at 27~28% lower stress, with 64~65% larger shear distance at the same load) after exposure to 2 Pa electron-beam excited H_2. In other words, hydrogen substantially enhances the screw dislocation motion in α-iron.

We further performed a stress analysis to elucidate if there is any relation between the changes in σ_c and δ_{max}. When a dislocation is bent into a curved shape with a radius of curvature r, a responsive opposite shear stress τ_{bow} arising from the dislocation line tension tends to straighten the dislocation back and the τ_{bow} at σ_{max} in each cycle can be calculated using the methods outlined in Supplementary Note 2 and Supplementary Fig. 6. Both τ_c and τ_{bow} act against the applied stress. Considering that the bowing dislocations only sweep a small area when in motion, we can assume that the local stress environment remains uniform, i.e., the long-range elastic interactions among the observed dislocations and other defects have negligible change. Under this assumption, we find that the sum of τ_c and τ_{bow} is almost identical (see Supplementary Fig. 7), indicating that the enlarged δ_{max} is a direct result of the reduced σ_c. Moreover, it was clearly shown that the fluctuations of the δ_{max} increased after hydrogenation, as indicated in Fig. 2d and 2e, where the measured standard deviation of the averaged δ_{max} was increased from ~0.6 to ~3.3 nm. Such increased fluctuations imply that the redistribution of hydrogen in the sample arising from the loading stress and from the position change of the dislocation is not exactly identical in all of the cycles. During loading, the compressive loading stress tends to drive hydrogen out of its trapping positions at dislocations and vacancies[30,34], entering the pillar volume and finally leaving the specimen into the surrounding environment. In contrast, if all lattice defects remain unchanged, the hydrogen is assumed to maintain its original distribution, as the thermal activation is below the trapping depth[37,38]. This type of load-driven hydrogen degassing thus seems to affect the observed dislocation motion.

It is worth noting that our experiments prove the hydrogen-enhanced screw dislocation motion only for the case of low hydrogen concentrations. With increasing hydrogen concentration, it is possible that other hydrogen effects might prevail, for instance in light of a recently published model that suggests that a hydrogen-drag effect on kink propagation will become the rate-limiting process for screw dislocation motion[15]. Under such circumstances, even hydrogen-inhibited screw dislocation motion was suggested to occur, based on simulations[15]. Indeed, our previous work has also experimentally shown hydrogen-inhibited dislocation motion in FCC aluminum[24], but via hydrogenated vacancies rather than directly via interstitial hydrogen atoms. Such hydrogenated vacancies have also been reported to affect kink pair nucleation and migration, thereby imposing large resistance to screw dislocations in BCC metals[30,39]. These different experimental results and simulation trends indicate that the hydrogen-dislocation interaction depends on the specific material probed, on the dislocation types that predominantly carry the deformation and also on the specific hydrogen and vacancy concentrations. In our study, the drag effect caused by hydrogenated vacancies is not dominant in the α-iron pillars. This means that not many superabundant vacancies had formed under the condition probed here (e.g., at the early stage of plastic deformation). However, this is not in contradiction to the theory of hydrogen enhanced strain-induced vacancy formation[4], as larger numbers of vacancies are in BCC metals mostly formed through the jog drag mechanisms, an effect less relevant at low and moderate strains.

Next, we changed the loading environment from hydrogen atmosphere back to vacuum, to see if the dislocation response under load could be reversed after switching the atmosphere back to vacuum. In the loading cycles in 2 Pa H_2 that followed $N = 12$ (see Supplementary Movie 2), the configuration of dislocation #1 changed due to an accidental depinning event. We thus had to increase the stress amplitude of the following loading session to introduce another similar dislocation (marked as #2 in Fig. 3a), turning it into a stable bow-out motion (see Supplementary Movie 5) using cyclic loading between σ_{min} (~35 MPa) and σ_{max} (~353 MPa), making it accessible for the following observation. The stress-induced change in shapes and positions of dislocation #2 in cycles before and after degassing are shown in Fig. 3b-d. Throughout all the 23 load cycles imposed during the testing session immediately before degassing, the stress-driven dislocation motion was almost the same, with average $\delta_{\mathrm{max}} = 6.2 \pm 0.5$ nm and $\sigma_{\mathrm{c}} = 182.3 \pm 20.8$ MPa. Then, the hydrogen inlet was closed, and within only two minutes, the specimen chamber of the ETEM was pumped to high vacuum (< 5×10^{-4} Pa). In the following 3 hours, the sample stayed under vacuum for further degassing. Such a long degassing time is sufficient for the hydrogen in the sample to assume a new equilibrium distribution. After degassing, we applied the same cyclic load and observed that in the first cycle, the dislocation moved to almost the same δ_{max} as that in the cycles before degassing, but in the ensuing 8 load cycles, the average δ_{max} of dislocation #2 gradually decreased, from 6.2 nm to 1.8 nm (see Fig. 3b-f and Supplementary Movie 6). Meanwhile, the measured σ_{c} after degassing remained at the first reload cycle and then gradually increased until reaching a plateau value of 321±7 MPa after the 9th cycle, showing a ~43% lower activation stress σ_{c} in hydrogenated state than in its hydrogen-free state (Fig. 3e and 3f). These results demonstrate the fully reversible nature of the hydrogen-dislocation interaction, consistent with the recovery of conventional plastic flow observed in bulk metals with low hydrogen concentration after degassing[5].

We also note that the recovery of dislocation response after switching back to vacuum is unexpectedly slow, since even after ~3 hours of degassing in vacuum, it still takes ~20 seconds, or ~10 load cycles, for dislocation #2 to gradually recover its stable cyclic motion under vacuum. Due to the high diffusivity of hydrogen in α-iron (D_{H}, of the order of 10^{-9}~10^{-8} $\mathrm{m^2 \cdot s^{-1}}$ at room temperature[40]), the time for hydrogen to diffuse out of the pillar (approximated by $L^2/4D_{\mathrm{H}}$, where $L \sim 1000$ nm is the characteristic length scale) is estimated to be less than 1 second. This means that the time lapse (2 s) during each individual load cycle is sufficient for hydrogen to redistribute and reach a new equilibrium distribution inside the pillar. Given the fact that the full restoration of the dislocation behavior after switching from hydrogen back to vacuum requires multiple load cycles, hydrogen traps should play a critical role in the overall recovery kinetics. Even after hours of aging under vacuum condition, the traps can still retain a certain amount of hydrogen, which is released only slowly during the ensuring load cycles, so that its effect on dislocation motion remains active until the hydrogen stored in these traps is gradually decreased below a critical level. Considering that no strong hydrogen traps, such as grain boundaries or precipitates, are present in our sample, the delayed restoration of the dislocation behavior must originate from other traps, such as dislocations or vacancies[30,37,38].

One possibility to explain this phenomenon of delayed hydrogen release and the observed gradual restoration of the dislocation behavior is the de-trapping of hydrogen from dislocations during their motion (rather than from vacancies), due to the following reasons. On the one hand, hydrogen in α-iron has a lower binding energy at the screw dislocation core ($E_{\mathrm{H-screw}}$ = 0.26~0.29 eV) compared to vacancies ($E_{\mathrm{H-Vac}}$ = 0.56~0.64 eV)[38,41], thus making hydrogen detachment from screw dislocation easier. On the other hand, vacancies are almost immobile under the stresses applied here, due to their spherical stress field which is insensitive to shear stresses, while screw dislocations readily move upon shear loading by nucleation, propagation and annihilation of kink pairs, thus helping to shake off the attached hydrogen. The fact that the hydrogen-induced enhancement in dislocation motion gradually faded with successive oscillating motion of the dislocations also indicates that for each load cycle, only a small part of the attached hydrogen atoms was shaken off, and thus multiple load cycles are required to exhaust the weakly trapped hydrogen from the screw dislocation lines. Also, as the motion of screw dislocations requires kink pairs, which have edge character, and some of the hydrogen can become re-trapped at these kinks, before finally being shaken off with repeated cycling. Such mechanically-assisted degassing effect suggests that to further eliminate dissolved hydrogen in metals and alloys, mechanical treatment can be an effective auxiliary option, in addition to traditional thermal annealing treatments. This means that the mitigation or even elimination of the hydrogen-enhanced local plasticity effect is only possible when hydrogen trapped at dislocations is ‘shaken off’ by cyclic mechanical loading. In order to better understand the trapping and removal at and from the core of screw dislocations, respectively, we further analyzed these phenomena by atomistic simulations.

To identify the underlying mechanisms of hydrogen-enhanced dislocation motion, we performed atomistic simulations based on the nudged elastic band (NEB)[42,43] approach. The NEB method allows us to identify minimum energy paths (MEPs) between known configurations and associated activation energies. The simulations were here used to study the elementary process of thermally activated screw dislocation motion in the absence and presence of a hydrogen atom, respectively. The simulation setup is shown in Supplementary Fig. 8. The NEB results in Fig. 4a reveal the representative MEPs of screw dislocation glide under the resolved shear stress τ_{yz} = 24 MPa (Supplementary Note 3). Similar to previous reports about the glide of screw dislocations in BCC metals without hydrogen[44,45], it is the correlated kink pair nucleation that controls the activation mechanism. Furthermore, the hydrogen atom breaks the symmetry of the screw dislocation core region and in this way can serve as an energetically favorable site for kink nucleation (see Fig. 4b and 4c), leading to a lower energy barrier (from E = 0.47 eV without hydrogen to E_{H} = 0.42 eV with hydrogen) for screw dislocation glide. Supplementary Fig. 9 demonstrates the stress-dependent activation energies, revealing that the reduction of the energy barrier ($\Delta E = E - E_{\mathrm{H}}$ = 0.05 eV) is not sensitive to the resolved shear stress range studied (τ_{yz} = 0~58 MPa).

Earlier atomistic calculations have shown that the trapping of a hydrogen atom in the kink is expected to be stronger than that in the kink-free dislocation core, thus lowering the Peierls barrier of kink nucleation[29,30]. We further unveiled the atomistic mechanism of the binding energy difference of hydrogen at various positions via tracking the intermediate atomic configurations of the kink nucleation process around the hydrogen atom, as shown in Fig. 4f and 4g. We find that the size of the interstice available for accommodating the hydrogen atom, i.e., the volume of a polyhedron (Ω_H) consisting of six nearest iron atoms around hydrogen, increases from 12.4 $Å^3$ to 13.4 $Å^3$ for a hydrogen atom in its saddle-point configuration (Fig. 4g) compared to that in its initial relaxed configuration (Fig. 4f). When viewed along the dislocation line (positive Z direction), the atomic rows around the hydrogen atom vary from strong clockwise chirality[46] (1→2→3) to weak counter-clockwise chirality (1→3→2), which is close to the hard-core configuration with the largest size of interstitial site[30] accommodating the hydrogen atom. The larger size of interstice volume for hydrogen in the saddle-point configuration results in the larger binding energy compared to its binding energy in the initial relaxed configuration, leading to the reduced kink nucleation barrier. Also, such a positive activation volume and strong binding energy imply a positive hydrogen Gibbs excess Γ_H^* at the saddle state relative to the ground state, further reducing the activation free energy by applying the Gibbs adsorption equation to the activated state[47]. Thus the hydrogen atoms promote kink nucleation and decrease the critical stress of dislocation glide. This effect has also been validated via our molecular dynamics (MD) simulations. Fig. 4h demonstrates the MD results for dislocation glide, with and without hydrogen atoms at room temperature. It is found that in the presence of randomly distributed hydrogen atoms (0.4 hydrogen atom per nanometer), the critical shear stress decreases from 32 MPa to 22 MPa, which is qualitatively consistent with our experimental results, i.e., τ_c of dislocation #1 reduces from 49.4 MPa to 35.6 MPa.

To recapitulate, we have demonstrated that after exposing α-iron to 2 Pa H_2, the critical stress for activating the motion of screw dislocations was reduced by 27~43% while the maximum glide distance of the bow-out motion was enhanced by >64%. At first glance, these results resemble the conclusions from the classic works of Birnbaum, Robertson and coworkers[19–23], revealing that hydrogen promotes dislocation motion, leading to hydrogen-enhanced local plasticity[2]. However, compared with the experimental setups used in these earlier works, the experimental setup introduced here offers a few major differences. Firstly, our setup allows to run the experiments in such a way that either hydrogen-induced inhibition (solute-drag or pinning effects) or hydrogen-induced promotion for dislocation motion is possible to be observed (Fig. 1d). Secondly, our samples are charged under a load-free state with low gas pressure and the subsequent reloading was carefully calibrated to be exactly the same as before hydrogen charging. Finally, in the current study the same set of pinning points were maintained throughout the loading and hydrogen charging experiments, thus leaving the basic dislocation configuration unaffected in its bow-out motion. Hence, we were able to perform in situ mechanical experiments under varying environmental conditions with a novel approach that allows a painstakingly precise control of all boundary conditions by reducing undesired influences from surface pinning and local stress changes, thereby obtaining unequivocal experimental evidence for hydrogen-enhanced screw dislocation motion.

In non-hydride-forming metals, the HELP mechanism, as one of the most important HE mechanisms, is regarded as a key mechanism contributing to HE, as frequently revealed by metallographic features stemming from enhanced dislocation activity beneath either intergranular or transgranular fracture surfaces in iron and steels[7,48]. One critical element of the HELP model is the hydrogen-enhanced dislocation activity (e.g. mobility) at the early and intermediate stages of deformation, prior to the formation of microvoids. This is usually interpreted as a result of the elastic shielding effect, which has been proposed on the basis of experimental observations that reported hydrogen-induced reduction in the spacing among piled-up edge dislocations[31]. In this work, we provide a compelling piece of evidence of another factor contributing to the increase in dislocation activity, namely, hydrogen-enhanced screw dislocation motion in α-iron. We show that this effect arises from the reduction of the kink nucleation barrier during screw dislocation glide.

On the application side, we have introduced an additional novel hydrogen removal and degassing strategy by modest mechanical cycling, which can help further remove hydrogen atoms still attached to dislocations after vacuum or thermal degassing. Such mechanical degassing has certain advantages over the conventional thermal degassing practice, as it confines to a minimum influence of the degassing effect on the microstructure and thus on the mechanical properties, making this approach highly suited as a new degassing protocol in industrial practice.

Methods

Sample preparation. Rectangular lamellae with dimensions of ~30 × 20 × 5 μm^3 were cut from a one-side polished single crystalline α-iron disk (where the purity of the used iron was ~ 99.99%) using a focused ion beam instrument (FIB) FEI Helios NanoLab 600, operated at 30 keV. The so prepared sample was then transferred and mounted to a mechanical testing rig employing the built-in FIB lift-out system. The cylindrical pillars with an aspect ratio (length/diameter) of ~3 were fabricated on the lift-out lamellae using the same FIB instrument. To minimize any potentially harmful side effects stemming from the Ga^+ beam induced irradiation damage and geometrical tapering of the sample longitudinal shape, the milling current in the final step was reduced to values below 20 pA.

In situ mechanical tests. All mechanical in situ tests were carried out inside of a Hitachi H-9500 ETEM using a Hysitron PI95 H1H sample holder. The holder was equipped with a flat diamond punch which was driven by a Micro-electromechanical Systems (MEMS) transducer. The transducer operated at a force resolution of ~300 nN and a displacement resolution of ~2 nm. Both, the mechanical loading direction and the electron-beam direction were oriented along the <100> crystallographic axis of the α-iron sample. Monotonic uniaxial compression tests were performed under displacement control mode at a strain rate of ~ $5\times10^{-3}\ s^{-1}$. The cyclic compression and relaxation tests were conducted in load control mode, and the period of each cycle was 2 s (1.0 s loading + 1.0 s unloading). The applied stress that was imposed during each cycle oscillated from a low valley stress to a peak stress to carefully and stepwise manipulate the movement of the mobile dislocations. Hydrogenation of the pillar was conducted under an electron-beam intensity of ~1.2 nA μm^{-2} in a 2 Pa H_2 environment. Degassing lasted over a period of 3 hours under high vacuum (< 5×10^{-4} Pa) under switched-off electron-beam conditions. Real-time movies of the in situ mechanical tests were recorded using a Gatan 832 CCD camera, operated at an image acquisition rate of 10 frames per second.

Atomistic simulations. Supplementary Fig. 8 shows the 3D simulation cell containing a right-hand screw dislocation at its fully relaxed ground state. Relaxation was conducted by the conjugate gradient method at 0 K. The simulation cell had dimensions of 5.6 × 5.6 × 47.5 nm^3 and contained a total number of ~80,000 atoms. A periodic boundary condition was imposed along the dislocation line (Z-[111] direction), while the surfaces along the X-$[\bar{2}11]$ and Y-$[0\bar{1}1]$ directions were maintained traction-free. Two 0.6-nm-thick slabs were fixed at the two ends of the simulation cell in the Y direction. The shear stress required to move the dislocation was exerted by imposing a displacement-controlled boundary condition on the top slab, while the bottom slab was held fixed. We performed NEB calculations in conjunction with an embedded atom method (EAM) potential of FeH[41] using the atomistic simulation toolbox LAMMPS[49]. MD simulations were also performed at room temperature for the same simulation setup. The constant shear strain rate of 1×10^{8} s^{-1} was exerted in the canonical ensemble (NVT). The hydrogen atoms were randomly embedded into the region around dislocation core in the simulation cell. To obtain average virial stress, we performed 20 independent MD simulations using the NVT ensemble with random initial velocities. The visualisation tool OVITO[50] was employed to perform common neighbour analysis to clearly display the screw dislocation.

Data availability

The data that support the findings of this study are available from the corresponding authors upon reasonable request.

Declarations

Acknowledgement

The authors acknowledge supports from Natural Science Foundation of China (52031011and 51971169), Shaanxi Postdoctoral Science Foundation (2017JQ5110). D.K. acknowledges the support from Shanghai Pujiang Program (21PJ1404800). The authors would like to thank Z. Wang (Xi’an Jiaotong University), S. Ogata (Osaka University), C. Zhou and L. Zhang (Zhejiang University of Technology), L. Qiao and Y. Su (University of Science and Technology Beijing) for useful discussions. The authors also thank Y. Qin, D. Zhang, P. Zhang, C. Guo and Q. Fu for assistance in sample preparation and guidance for doing TEM experiments.

Author contributions

Z.S. and D.X. designed and supervised the project. L.H. and D.X. conducted the experiments and analyzed the experimental data. D.C. performed the simulations under guidance of T.Z., L.H., D.X. and D.C wrote the paper with input from Z.S., E.M., J.L., T.Z. and D.R. All authors contributed to discussions of the results and the revision of manuscript.

Competing financial interests. The authors declare no competing financial interests.

References

1. Beachem, C. D. A new model for hydrogen-assisted cracking (hydrogen 'embrittlement'). *Metall. Mater. Trans. B* **3**, 441–455 (1972).
2. Birnbaum, H. K. & Sofronis, P. Hydrogen-enhanced localized plasticity—a mechanism for hydrogen-related fracture. *Mater. Sci. Eng. A* **176**, 191–202 (1994).
3. Oriani, R. A. A mechanistic theory of hydrogen embrittlement of steels. *Ber. Bunsenges. Phys. Chem.* **76**, 848–857 (1972).
4. K. Sakaki, T. Kawase, M. Hirato, M. Mizuno, H. Araki, Y. Shirai, M. Nagumo, The effect of hydrogen on vacancy generation in iron by plastic deformation. *Scr. Mater.* **55**, 1031–1034 (2006).
5. Kimura, A. & Birnbaum, H. K. Plastic softening by hydrogen plasma charging in pure iron. *Scr. Metall. Mater.* **21**, 53–57 (1987).
6. Matsui, H., Kimura, H. & Moriya, S. The effect of hydrogen on the mechanical properties of high purity iron I. Softening and hardening of high purity iron by hydrogen charging during tensile deformation. *Mater. Sci. Eng.* **40**, 207–216 (1979).
7. Martin, M. L., Dadfarnia, M., Nagao, A., Wang, S. & Sofronis, P. Enumeration of the hydrogen-enhanced localized plasticity mechanism for hydrogen embrittlement in structural materials. *Acta Mater.* **165**, 734–750 (2019).
8. Gong, P., Nutter, J., Rivera-Diaz-Del-Castillo P. E. J. & Rainforth, W. M. Hydrogen embrittlement through the formation of low-energy dislocation nanostructures in nanoprecipitation-strengthened steels. *Sci. Adv.* **6**, eabb6152 (2020).
9. Birenis, D., *et al.* Interpretation of hydrogen-assisted fatigue crack propagation in BCC iron based on dislocation structure evolution around the crack wake. *Acta Mater.* **156**, 245–253 (2018).
10. Song, J. & Curtin, W. A. Atomic mechanism and prediction of hydrogen embrittlement in iron. *Nat. Mater.* **12**, 145–151 (2013).
11. Wang, S., Hashimoto, N. & Ohnuki, S. Hydrogen-induced change in core structures of {110}[111] edge and {110}[111] screw dislocations in iron. *Sci. Rep.* **3**, 2760 (2013).
12. Koyama, M., *et al.* Origin of micrometer-scale dislocation motion during hydrogen desorption. *Sci. Adv.* **6**, eaaz1187 (2020).
13. Yin, S., *et al*. Hydrogen embrittlement in metallic nanowires. *Nat. Commun.* **10**, 2004 (2019).

14. Katzarov, I. H., Pashov, D. L. & Paxton, A. T. Hydrogen embrittlement I. Analysis of hydrogen-enhanced localized plasticity: Effect of hydrogen on the velocity of screw dislocations in α-Fe. *Phys. Rev. Mater.* **1**, 033602 (2017).
15. Kirchheim, R. Solid solution softening and hardening by mobile solute atoms with special focus on hydrogen. *Scr. Mater.* **67**, 767–770 (2012).
16. Yu, P., Cui, Y., Zhu, G., Shen, Y. & Wen, M. The key role played by dislocation core radius and energy in hydrogen interaction with dislocations. *Acta Mater.* **185**, 518–527 (2020).
17. Cottrell, A. H. & Bilby, B. A. Dislocation theory of yielding and strain ageing of iron. *Proc. Phys. Soc. Sect. A* **62**, 49-62 (1949).
18. G. Schoeck, G. & Seeger, A. The flow stress of iron and its dependence on impurities. *Acta Metall.* **7**, 469–477 (1959).
19. Shih, D. S., Robertson, I. M. & Birnbaum, H. K. Hydrogen embrittlement of α titanium: In situ tem studies. *Acta Metall.* **36**, 111–124 (1988).
20. Bond, G. M., Robertson, I. M. & Birnbaum, H. K. Effects of hydrogen on deformation and fracture processes in high-ourity aluminium. *Acta Metall.* **36**, 2193–2197 (1988).
21. Matsumoto, T., Eastman, J. & Birnbaum, H. K. Direct observations of enhanced dislocation mobility due to hydrogen. *Scr. Metall. Mater.* **15**, 1033–1037 (1981).
22. Rozenak, P., Robertson, I. M. & Birnbaum, H. K. HVEM studies of the effects of hydrogen on the deformation and fracture of AISI type 316 austenitic stainless steel. *Acta Metall. Mater.* **38**, 2031–2040 (1990).
23. Tabata, T. & Birnbaum, H. K. Direct observations of the effect of hydrogen on the behavior of dislocations in iron. *Scr. Metall. Mater.* **17**, 947–950 (1983).
24. Xie, D., *et al.* Hydrogenated vacancies lock dislocations in aluminium. *Nat. Commun.* **7**, 13341 (2016).
25. Song, J. & Curtin, W. A. Mechanisms of hydrogen-enhanced localized plasticity: An atomistic study using α-Fe as a model system. *Acta Mater.* **68**, 61–69 (2014).
26. Vitek, V. Core structure of screw dislocations in body-centred cubic metals: relation to symmetry and interatomic bonding. *Philos. Mag.* **84**, 415–428 (2004).
27. Maresca, F., Dragoni, D., Csányi, G., Marzari, N. & Curtin, W. A. Screw dislocation structure and mobility in body centered cubic Fe predicted by a Gaussian Approximation Potential. *NPJ Comput. Mater.* **4**, 69 (2018).
28. Hirth, J. P. Effects of hydrogen on the properties of iron and steel. *Metall. Trans. A* **11**, 861–890 (1980).
29. Wen, M., Fukuyama, S. & Yokogawa, K. Atomistic simulations of effect of hydrogen on kink-pair energetics of screw dislocations in bcc iron. *Acta Mater.* **51**, 1767–1773 (2003).
30. Itakura, M., Kaburaki, H., Yamaguchi, M. & Okita, T. The effect of hydrogen atoms on the screw dislocation mobility in bcc iron: a first-principles study. *Acta Mater.* **61**, 6857–6867 (2013).

31. Robertson, I. M. The effect of hydrogen on dislocation dynamics. *Eng. Fract. Mech.* **68**, 671–692 (2001).
32. Barnoush, A. Hydrogen embrittlement. *Thesis. Saarbrücken: Saarland University* (2011).
33. Wang, Z., *et al.* Cyclic deformation leads to defect healing and strengthening of small-volume metal crystals. *Proc. Nat. Acad. Sci. U. S. A.* **44**, 13502–13507 (2015).
34. Bacon, D. J., Osetsky, Y. N. & Rodney, D. Dislocation–obstacle interactions at the atomic level. In: *Dislocations in Solids*, Vol. 15 (eds Hirth J. P., Kubin L.), 1-90 (Elsevier, 2009).
35. Bond, G. M., Robertson, I. M. & Birnbaum, H. K. On the determination of the hydrogen fugacity in an environmental cell TEM facility. *Scr. Metall. Mater.* **20**, 653–658 (1986).
36. Xie, D., *et al*. *In situ* study of the initiation of hydrogen bubbles at the aluminium metal/oxide interface. *Nat. Mater.* **14**, 1–6 (2015).
37. Tateyama, Y. & Ohno, T. Stability and clusterization of hydrogen-vacancy complexes in α – Fe:An ab initio study. *Phys. Rev. B* **67**, 174105 (2003).
38. Kimizuka, H. & Ogata, S. Slow diffusion of hydrogen at a screw dislocation core in α-iron. *Phys. Rev. B* **84**, 024116 (2011).
39. Zhang, B., *et al.* Atomic modeling of the segregation of vacancies on <111> dislocations in α-iron by diffusive molecular dynamics simulations. *J. Alloys Compd.* **857**, 157486 (2021).
40. Cheng, B., Paxton, A. T. & Ceriotti, M. Hydrogen diffusion and trapping in α-iron: The role of quantum and anharmonic fluctuations. *Phys. Rev. Lett.* **120**, 225901 (2018).
41. Ramasubramaniam, A., Itakura, M. & Carter, E. A. Interatomic potentials for hydrogen in α–iron based on density functional theory. *Phys. Rev. B* **79**, 174101 (2009).
42. Zhu, T., Li, J., Samanta, A., Leach, A. & Gall, K. Temperature and strain-rate dependence of surface dislocation nucleation. *Phys. Rev. Lett.* **100**, 025502 (2008).
43. Chen, D., Costello, L. L., Geller, C. B., Zhu, T. & McDowell, D. L. Atomistic modeling of dislocation cross-slip in nickel using free-end nudged elastic band method. *Acta Mater.* **168**, 436–447 (2019).
44. Gordon, P., Neeraj, T., Li, Y. & Li, J. Screw dislocation mobility in BCC metals: the role of the compact core on double-kink nucleation. *Modell. Simul. Mater. Sci. Eng.* **18**, 085008 (2010).
45. Narayanan, S., McDowell, D. L. & Zhu, T. Crystal plasticity model for BCC iron atomistically informed by kinetics of correlated kinkpair nucleation on screw dislocation. *J. Mech. Phys. Solids* **65**, 54–68 (2014).
46. Trinkle, D. R. & Woodward, C. The chemistry of deformation: How solutes soften pure metals. *Science* **310**, 1665–1667 (2005).
47. Du, J.-P., Geng, W. T., Arakawa, K., Li, J. & Ogata, S. Hydrogen-enhanced vacancy diffusion in metals. *J. Phys. Chem. Lett.* **11**, 7015–7020 (2020).
48. Sun, B, *et al.* Chemical heterogeneity enhances hydrogen resistance in high-strength steels. *Nat. Mater.* (2021). https://doi.org/10.1038/s41563-021-01050-y

49. Plimpton, S. Fast parallel algorithms for short-range molecular dynamics. *J. Comput. Phys.* **117**, 1–19 (1995).

50. Stukowski, A. Visualization and analysis of atomistic simulation data with OVITO–the Open Visualization Tool. *Modell. Simul. Mater. Sci. Eng.* **18**, 015012 (2009).

Figures

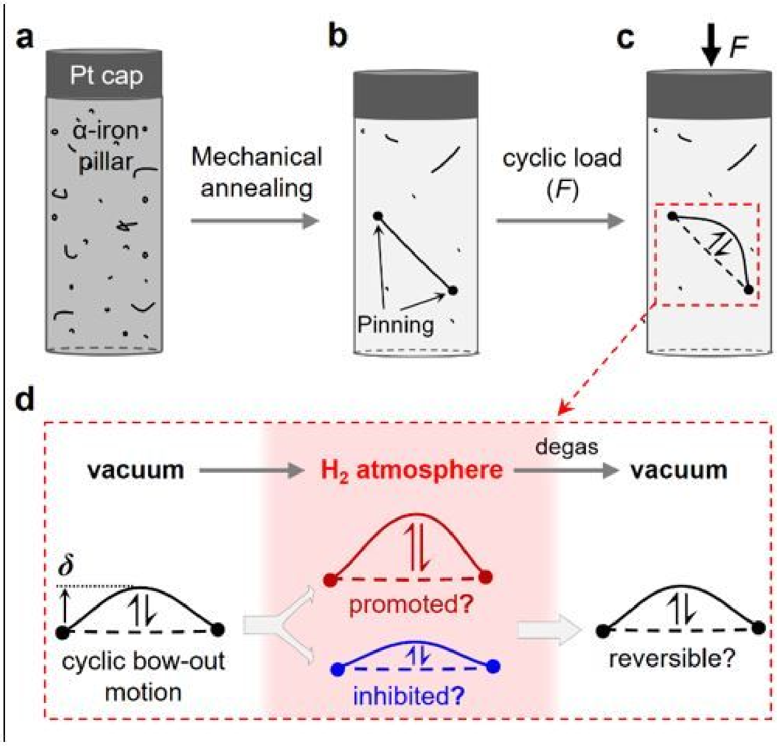

Fig. 1 | Schematic of the experimental setup for revealing the effect of hydrogen on dislocation motion. (**a**) The as-fabricated single-crystal iron pillar with a platinum cap at the top, to provide well-controlled contact conditions. (**b**) The pillar after mechanical annealing treatment (see in the text), which eliminates most pre-existing dislocations while retaining several long screw-type dislocations with both ends pinned. (**c**) Under cyclic compression loads (*F*) with engineering stress ranging from the minimum ($\sigma_{\min}$) to the maximum ($\sigma_{\max}$), dislocation segments between pinning points accordingly move forward and back. The dashed lines show their shape/position at $\sigma_{\min}$. (**d**) The sequential cyclic compression experiments under varying testing atmosphere (vacuum, hydrogen) to compare the dislocation motion under well-defined mechanical and atmospheric boundary conditions.

Figure 1

See image above for figure legend

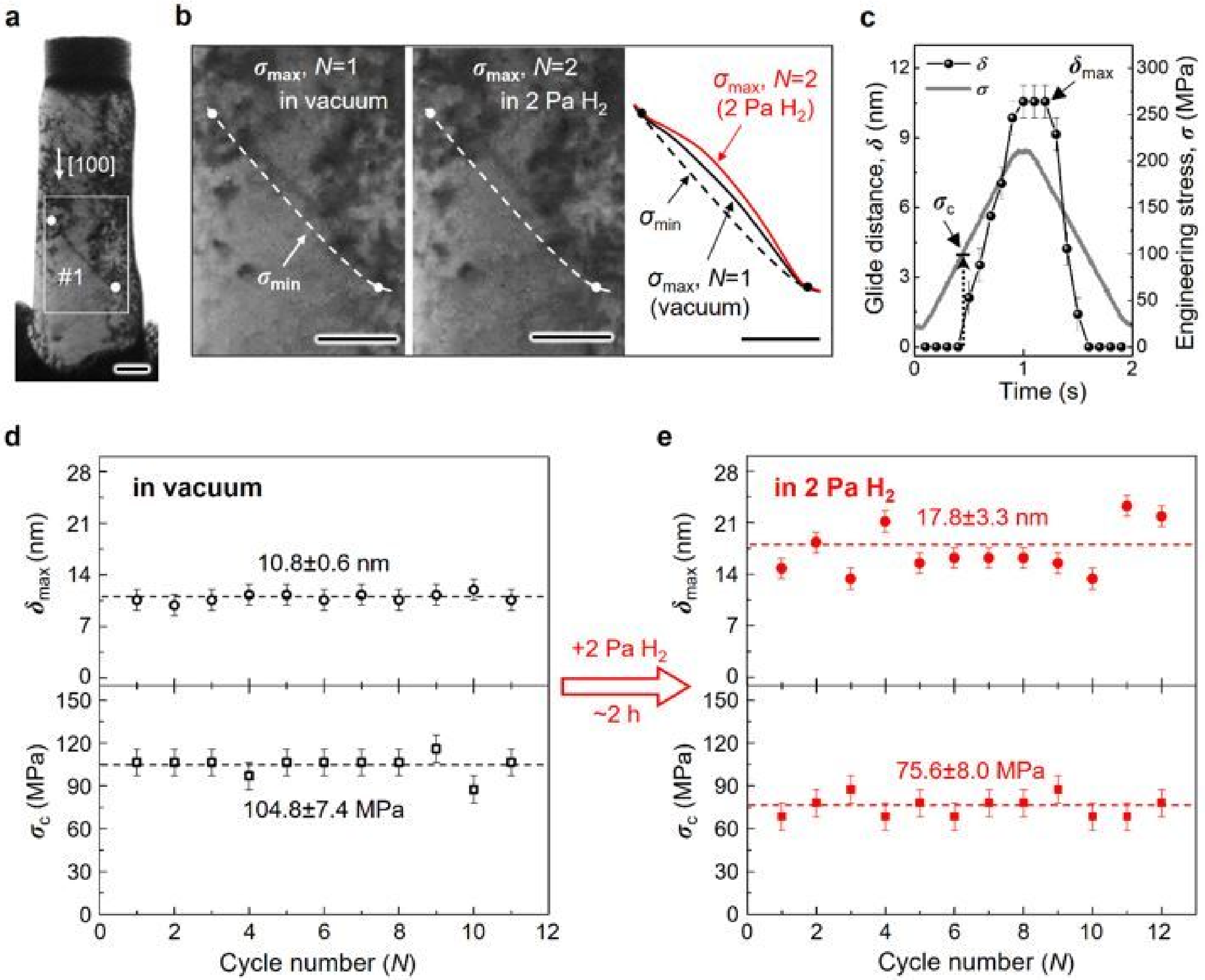

Fig. 2 | Effect of hydrogenation on the bow-out motion of a screw dislocation. (**a**) Bright Field TEM image showing the pillar after a series of cyclic compression loading/unloading sessions (as detailed in Supplementary Fig. 1). A mobile dislocation tagged as #1 in the boxed region is magnified and observed in (b). The white spots indicated the pinning points. (**b**) Configurations of dislocation #1 at σ_{max} in vacuum (N = 1) and in 2 Pa H_2 (N = 2), respectively. The shape and position of dislocation #1 at σ_{min}, which is the same as that under the unloaded state, as shown in (a), is delineated with a white dashed line and used as a reference position/shape. The superimposed profiles of dislocation #1 in different states are illustrated on the rightmost. (**c**) The loading engineering stress σ and the digitally tracked projected glide distance δ of dislocation#1 in a typical load cycle are shown as a function of time. The critical stress for activating the dislocation (σ_c) and the maximum glide distance (δ_{max}) are also indicated. (**d**) and (**e**) The measured δ_{max} and σ_c of dislocation #1 as a function of loading cycle number in vacuum, and in 2 Pa H_2, respectively. The tests in 2 Pa H_2 were started after that the pillar had been exposed to the 2 Pa H_2 atmosphere for ~2 hours. All scale bars are 100 nm.

Figure 2

See image above for figure legend

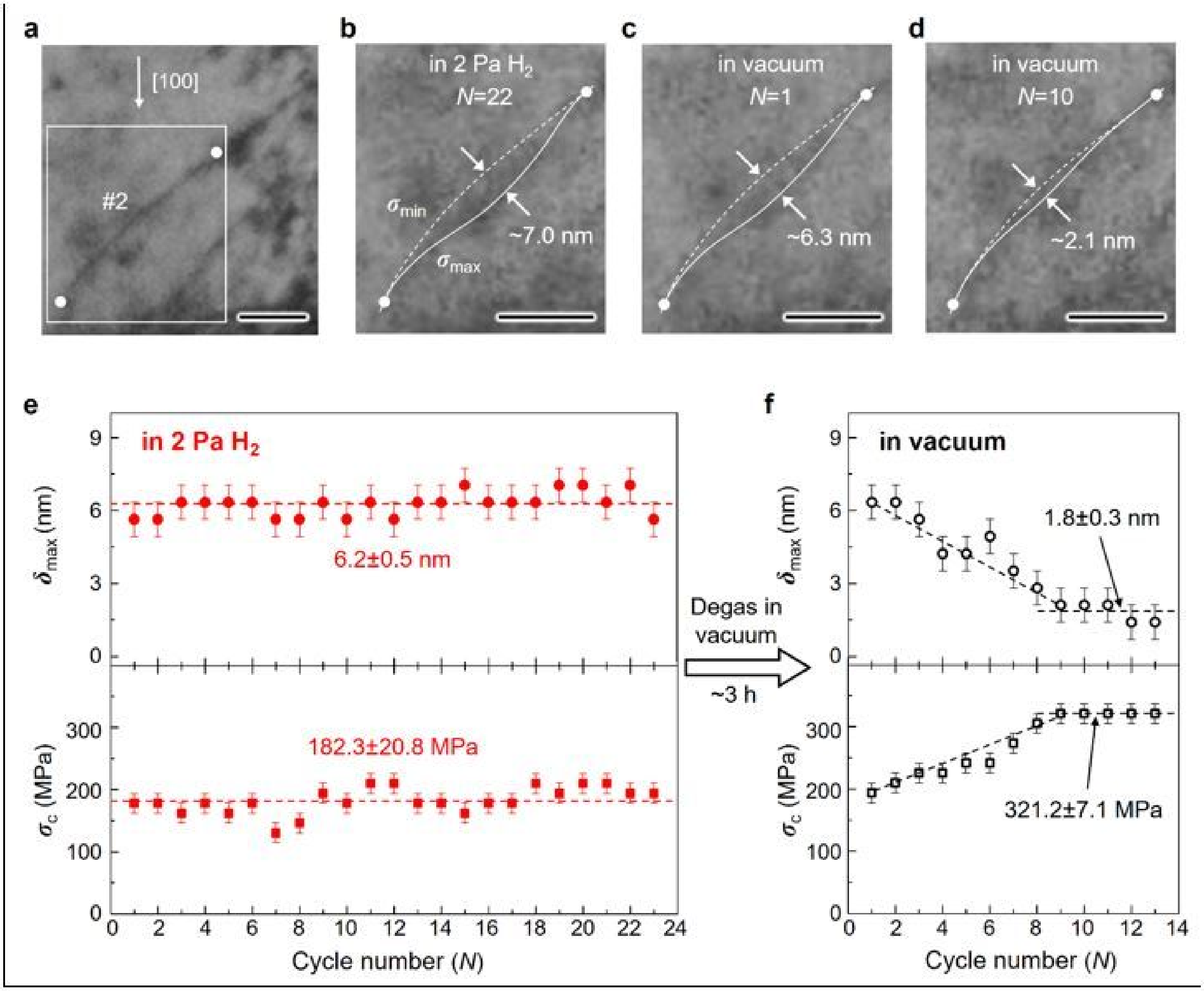

Fig. 3 | Effect of hydrogen degassing on the behaviors of dislocation. (**a**) Mobile dislocation #2 at σ_{min} (~35 MPa). The mobile segment of the dislocation #2 is located in the boxed area that is magnified and observed in (b)-(d), in which its profile is delineated as a white dashed line and used as a reference position/shape. (**b**-**d**) Dislocation motion of a few chosen cycles before (N = 22) and after (N = 1 and 10) switching back to vacuum. The profiles of dislocation #2 at σ_{max} (~355 MPa) are delineated with white solid lines. (**e**) and (**f**) The measured δ_{max} and σ_c of dislocation #2 in each cycle in vacuum, and in 2 Pa H_2, respectively. The tests in vacuum were started after that the sample had been degassed in vacuum for ~3 hours. All scale bars are 50 nm.

Figure 3

See image above for figure legend

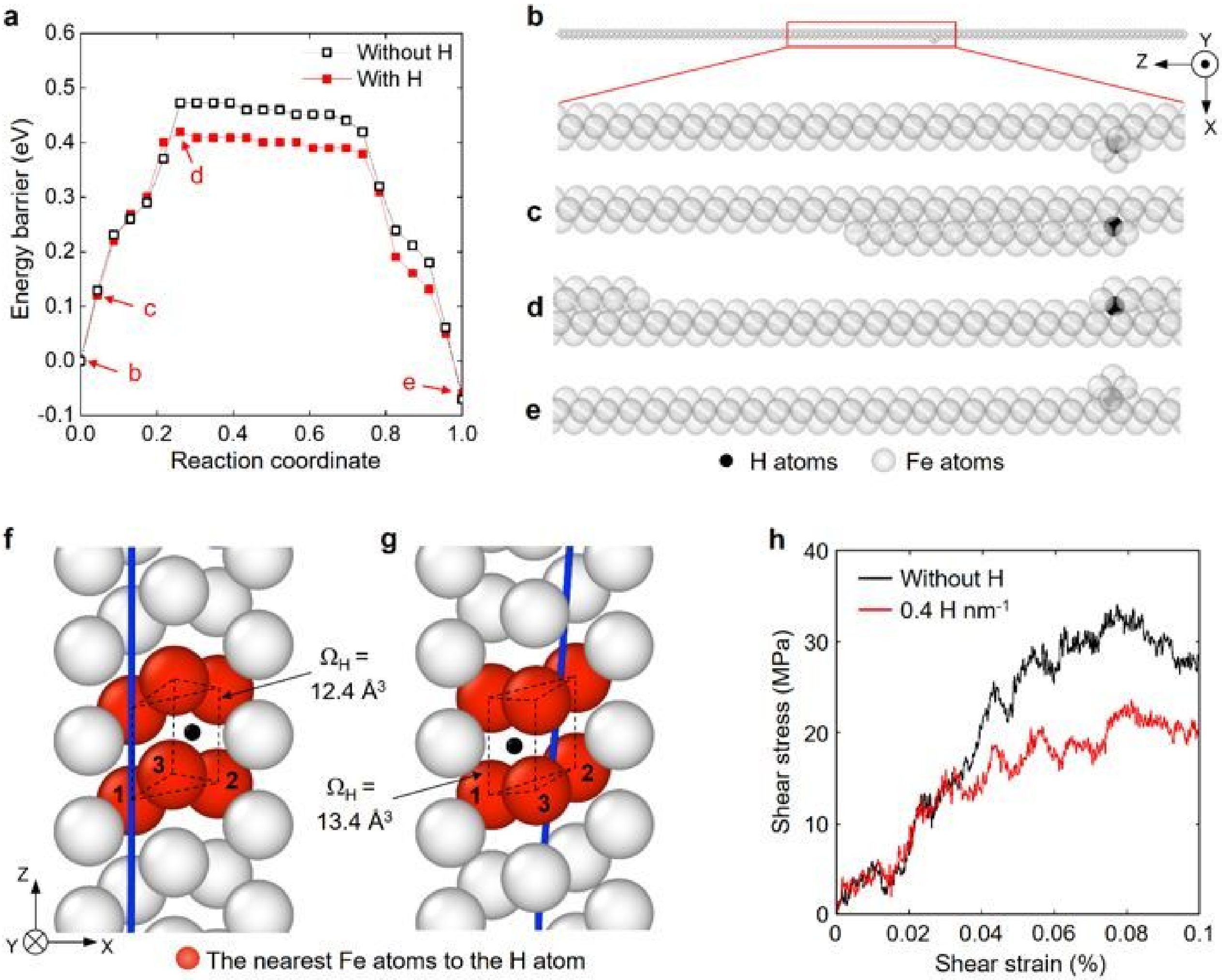

Fig. 4 | Atomistic mechanism of hydrogen-enhanced screw dislocation glide. (**a**) Representative MEPs of screw dislocation glide without/with a hydrogen atom under the resolved shear stress $\tau_{yz} = 24$ MPa. (**b**)-(**e**) Top view (along Y-direction) of atomic configurations of kink nucleation in the presence of a hydrogen atom. Their corresponding energies are plotted as red solid squares in (a). Here the hydrogen atom is denoted by a black sphere; the iron atoms are denoted by white-gray spheres. (**f**) and (**g**) The detailed atomic configurations around the hydrogen atom at the initial relaxed state and at the saddle-point state, respectively. Their corresponding energies are plotted as red solid squares marked with b and d in (a), respectively. Here the nearest iron atoms are labeled with red color. The dislocation is denoted by a blue line. (**h**) MD simulations results of mean stress-strain curves without/with hydrogen atoms.

Figure 4

See image above for figure legend

Supplementary Files

This is a list of supplementary files associated with this preprint. Click to download.

- FeH1108NatmatSI.docx
- MovieS1.mp4
- MovieS6.mp4
- MovieS2.mp4
- MovieS4.mp4
- MovieS3.mp4
- MovieS5.mp4